ACS APPLIED MATERIALS & INTERFACES

www.acsami.org

Research Article

Niobium Carbide and Tantalum Carbide as Nitrogen Reduction Electrocatalysts: Catalytic Activity, Carbophilicity, and the Importance of Intermediate Oxidation States

Samar Alhowity,[†] Kabirat Balogun,[†] Ashwin Ganesan, Colton J. Lund, Olatomide Omolere, Qasim Adesope, Precious Chukwunenye, Stella C. Amagbor, Fatima Anwar, M. K. Altafi, Francis D'Souza, Thomas R. Cundari, and Jeffry A. Kelber*

Cite This: *ACS Appl. Mater. Interfaces* 2024, 16, 2180−2192

Read Online

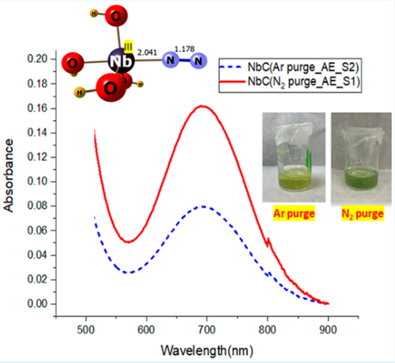

ABSTRACT: Significant interest in the electrocatalytic reduction of molecular nitrogen to ammonia (the nitrogen reduction reaction: NRR) has focused attention on transition metal carbides as possible electrocatalysts. However, a fundamental understanding of carbide surface structure/NRR reactivity relationships is sparse. Herein, electrochemistry, DFT-based calculations, and *in situ* photoemission studies demonstrate that NbC, deposited by magnetron sputter deposition, is active for NRR at pH 3.2 but only after immersion of an ambient-induced Nb_2O_5 surface layer in 0.3 M NaOH, which leaves Nb suboxides with niobium in intermediate formal oxidation states. Photoemission data, however, show that polarization to −1.3 V vs Ag/AgCl restores the Nb_2O_5 overlayer, correlating with electrochemical measurements showing inhibition of NRR activity under these conditions. In contrast, a similar treatment of a sputter-deposited TaC sample in 0.3 M NaOH fails to reduce the ambient-induced Ta_2O_5 surface layer, and TaC is inactive for NRR at potentials more positive than −1.0 V even though a significant cathodic current is observed. A TaC sample with surface oxide partially reduced by Ar ion sputtering in UHV prior to *in situ* transfer to UHV exhibits a restored Ta_2O_5 surface layer after electrochemical polarization to −1.0 V vs Ag/AgCl. The electrochemical and photoemission results are in accord with DFT-based calculations indicating greater N≡N bond activation for N_2 bound end-on to Nb(IV) and Nb(III) sites than for N_2 bound end-on to Nb(V) sites. Thus, theory and experiment demonstrate that with respect to NbC, the formation and stabilization of intermediate (non-d^0) oxidation states for surface transition metal ions is critical for N≡N bond activation and NRR activity. Additionally, the Nb suboxide surface, formed by immersion in 0.3 M NaOH of ambient-exposed NbC, is shown to undergo reoxidation to catalytically inactive Nb_2O_5 at −1.3 V vs Ag/AgCl, possibly due to hydrolysis or other, as yet not understood, phenomena.

KEYWORDS: *niobium carbide, tantalum carbide, electrochemical nitrogen reduction reaction, carbophilicity, density functional theory, intermediate oxidation states, ammonia*

■ INTRODUCTION

Ammonia, critical for agriculture and of increased interest for energy applications, is currently produced by the high-temperature Haber−Bosch process, which accounts for almost 2% of world energy consumption and is a significant source of CO_2 production, due to the use of fossil fuels to achieve the necessary temperatures.[1,2] Earth-abundant transition metal carbides (due to their metallic nature and other properties) are of long-standing interest as catalysts and electrocatalysts[3−8] and as electrochemical supports.[9] However, a fundamental understanding of the evolution of carbide surface structures under electrochemical conditions and their relationship to NRR activity is lacking.[5,8] Kimmel et al., however, have reported that transition metal carbides, in general, can remain electrochemically active under acidic conditions, provided that any surface oxide formed by exposure to ambient[10] be removed by preliminary immersion in 0.3 M NaOH solution.[9]

Herein, electrochemistry, theory, and UHV-electrochemistry (UHV-EC) are used to probe both the NRR activities of NbC and TaC surfaces under acidic conditions after preliminary immersion in 0.3 M NaOH, and the relationship between NRR activities and the evolution of surface oxide structures at the electrolyte/carbide interface. UHV-EC incorporates *in situ* sample transfer between electrochemical and UHV environ-

Received: August 7, 2023
Revised: December 6, 2023
Accepted: December 12, 2023
Published: January 4, 2024

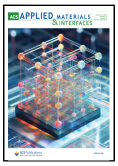

https://doi.org/10.1021/acsami.3c11683

ments under controlled conditions without exposure to ambient.[11] UHV-EC has proven valuable (despite unavoidable exposures to high pressure of water vapor during sample transfer) in correlating changes in the electrochemical environment (e.g., electrochemical potential) with changes in surface oxidation and other compositional aspects, even for non-noble materials, such as Fe [11] and V.[12]

As oxidation of the metal carbide surface and strength of M−O bonds (either in ambient or in solution) would appear to be a critical factor in determining electrocatalytic activity,[9] two different metals with near equal oxophilicity values of 0.8 [13] (Nb and Ta) were selected for initial examination. However, the experimental and theoretical results reported here indicate that other factors, including the relative stabilities of the respective oxides and carbides, are important in determining electrochemical behavior.

The experimental and theoretical results described herein demonstrate that although immersion in 0.3 M NaOH and rinsing in DI water immediately prior to insertion in N_2-purged electrolyte (pH 3.2) enable NRR activity in NbC at potentials more positive than −1.0 V vs Ag/AgCl, the same does not happen for TaC. UHV-EC results indicate that NRR activity is correlated with the effective removal of a Nb_2O_5 surface layer, leaving Nb(IV) and other oxides at the surface. NRR activity with varying Faradaic efficiency has been reported in the literature for various oxides of Nb.[14−18] Huang et al. reported significantly higher performance for NbO_2 compared to Nb_2O_5 due to the presence of d-electrons in Nb(IV) for N_2 triple bond activation.[15] In contrast to NbC, similar treatment of TaC does not remove the ambient exposure-induced Ta_2O_5 surface layer, and TaC is NRR inactive at similar potentials. (At potentials more negative than −1.0 V vs Ag/AgCl, slight NRR activity is observed for ambient exposed, NaOH-treated TaC, but see below.) DFT-based computations indicate that Nb and Ta in +4 and lower oxidation states are more effective at N≡N bond activation.[19] These calculations indicate the potential importance of metal d/N_2 π^* backbonding, suggesting experimental studies of NRR for other transition metal oxides with cations in d^0 vs non-d^0 oxidation states. Electrochemical and UHV-EC data reported here also show that at highly cathodic potentials, Nb_2O_5 regrowth occurs at the surface, thus limiting the effective potential range for NRR.

METHODS

Sample Deposition and Characterization. *Film Deposition.* NbC and TaC films were deposited by DC magnetron sputter deposition from corresponding sputter targets and characterized by *in situ* XPS in a system that permitted transport between deposition and analysis chambers under controlled vacuum conditions. This system is shown schematically in Figure S1 (Supporting Information). The base pressure of the turbomolecularly pumped sputter deposition chamber was 5×10^{-9} Torr. The surface analysis chamber has been described previously[20] and was equipped with a commercial dual anode (Mg Kα/Al Kα) nonmonochromatic X-ray source (Physical Electronics), 100 mm mean radius hemispherical analyzer (VSW) with multichannel detector (PSP Vacuum), and an ion sputter gun (PHI Ion Gun 04-191) for sample cleaning. Sputter deposition was carried out with a Meivac "MiniMak" DC magnetron source, with a source-to-substrate distance of 3 inches. A NbC sputter target (99.5% purity, 1.3 inches diameter, from Process Materials Inc.) and TaC sputter target (99.5% purity, 1.3 inches diameter, from Plasmaterials, Inc.) were used.

NbC and TaC films were deposited on commercially available fluorinated tin oxide (FTO) substrates. Prior to deposition, the 1 cm × 1 cm substrates were sonicated sequentially in soapy water, 0.1 M HCl, ethanol, acetone, and isopropyl baths and then dried with N_2 gas. After mounting in the vacuum system, substrates were cleaned by Ar^+ ion bombardment (1 keV, 5×10^{-5} Torr Ar partial pressure) to remove adventitious C and other contaminants. NbC deposition was carried out at a substrate temperature of ∼800 K in 8 mTorr Ar gas (Scott Specialty Gases, 99.9999% purity, CAS No. 7440-37-1) and 30 W power. TaC deposition was carried out at 800 K in 8 mTorr Ar gas and 25 W power. After short sputtering times, film thicknesses were estimated by intermittent sample transfer to the analysis chamber for XPS-derived estimation of film thickness via attenuation of the substrate Sn $3d_{5/2}$ signal. Initial deposition rates were then extrapolated to longer sputtering times to estimate the average thicknesses of deposited films.

Characterization by XPS. XPS spectra of freshly deposited films were acquired with the analyzer in constant pass energy mode, with a pass energy of 20 eV, using unmonochromatized Al Kα radiation. Measurements were generally carried out with the sample normal aligned with the analyzer axis: "normal emission". To enhance surface sensitivity, however, some spectra were acquired in "grazing emission" mode, with the sample normal inclined 60° with respect to the analyzer axis. XPS spectra were analyzed using commercial software (CasaXPS, version 2.3.24, Casa Software Ltd., U.K.) and standard methods.[21] Binding energy scales for NbC were calibrated by setting the C 1s binding energy for the carbidic feature at 282.7 eV.[22,23] For TaC, the corresponding C 1s carbide feature was set at 282.9 eV.[24,25] The spin−orbit doublet components of Nb 3d core level spectra ($3d_{5/2}$ and $3d_{3/2}$) were separated by 2.75 eV.[22,26] Spectral deconvolution was carried out with a constraint of 3:2 on the 5/2:3/2 peak intensities,[27,28] with Nb $3d_{7/2}$ binding energies as described in the literature[26,29] though allowed to vary slightly (<0.2 eV) for goodness of fit. A carbide phase C 1s binding energy of 282.9 eV was used to calibrate all the binding energies for TaC films.[24,25] The spin orbit doublet ($4f_{7/2}$ and $4f_{5/2}$) of Ta 4f spectra was separated by 1.9 eV.[30−32] Spectral deconvolution was set with a constraint of 4:3 on the 7/2:5/2 peak intensities.[30] Shirely background subtraction was applied to remove the background effect.[33,34]

Importantly, Nb metal and NbC have very similar 3d binding energies.[22,35] Initial calculations of Nb:C stoichiometry generally yielded an Nb:C atomic ratio of >1, indicating the presence of an Nb metal component in the surface region. Ar^+ ion sputtering was therefore carried out to remove surface Nb metal phases until the Nb:C atomic ratio was very close to 1.0. No such effect was observed for TaC films.

The decomposition of Nb 3d and Ta 4f XPS spectra is complicated by multiplet splittings and the presence of multiple oxidation states. Nb 3d spectra were decomposed using the assignments of Darlinksi et al.,[26] adjusted very slightly (within ±0.2 eV) with respect to binding energy to optimize fit, Table S1 (Supporting Information). Ta 4f binding energies for TaC and various oxides were similarly taken from the literature, with slight adjustments of binding energies to optimize fit, Table S2 (Supporting Information).

X-ray diffraction (XRD) measurements were performed *ex situ* on selected NbC and TaC films. XRD 2θ scans were obtained for several films using a Rigaku Ultima III Instrument employing Cu Kα radiation (λ = 1.541 Å). Scanning electron microscopy and energy dispersive X-ray spectroscopy (SEM/EDX) measurements were carried out on selected films using a JEOL JSM-IT200 electron microscope.

Electrochemical Methods. Measurements were performed in a three-electrode electrochemical cell and the electrolyte used was 0.1 M Na_2SO_4, adjusted with H_2SO_4 to a pH of 3.2. NbC and TaC immobilized on FTO were utilized as working electrodes for electrochemical analysis. A treatment solution was also prepared as 0.3 M NaOH, to remove or reduce oxides that may potentially form on the NbC and TaC films. The film was dipped in the 0.3 M NaOH solution for about 60 s and rinsed with DI water to remove the base. Experiments were carried out with an EG&G 263A potentiostat, having platinum and Ag/AgCl as counter and reference electrodes, respectively. The electrolyte was purged with N_2 or Ar and performed in 2 separate experiments. The gases were passed through 2 traps, one

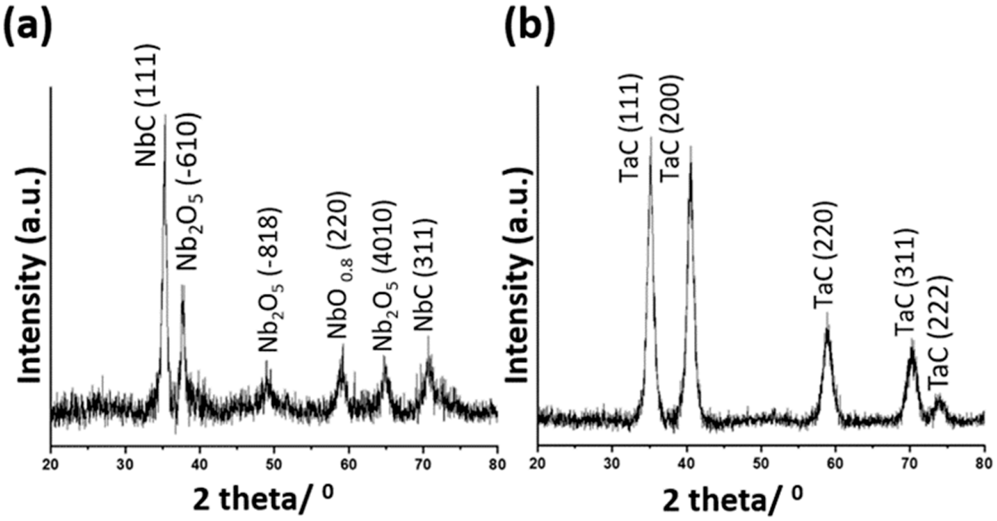

Figure 1. XRD 2θ scans of (a) NbC and (b) TaC films deposited under similar conditions.

with 0.1 M HCl and the other with 0.1 M KOH to remove contaminants like $NH_3/NO_2/NO_3$. Linear sweep voltammograms (LSVs) were recorded for both NbC and TaC on the reductive side under both N_2 and Ar environments to evaluate preliminary electrocatalytic activity. LSVs were also recorded for the NbC and TaC films after NaOH treatment to evaluate the difference in catalytic behavior.

To evaluate ammonia formation, the indophenol blue test was utilized. Electrolysis was performed for 90 min using the chronoamperometry technique in a 2-compartment cell, and Nafion membrane was placed between compartments. After the electrolysis, 10 mL of electrolyte was mixed with 0.5 mL of 0.55 M NaOH containing 5 wt % salicylic acid and sodium citrate, 100 μL of sodium nitroprusside dehydrate, and 100 μL of sodium hypochlorite to generate indophenol blue dye from the ammonia present in the solution. The mixture was kept without agitation at room temperature for 30 min, and the absorbance of the solution was measured using a JASCO V-670 spectrophotometer. The concentration of the ammonia formed in the experiment is calculated from calibration curves constructed for indophenol blue using standard concentrations of commercial liquid ammonia.

The ammonia yield after electrolysis at a defined potential (typically for 90 min) was quantified by calculation of the Faradaic efficiency,[15] or FE, according to the equation

$$\mathrm{FE} = \frac{n \cdot F \cdot C \cdot V}{M \cdot Q} \tag{1}$$

where n is the number of electrons produced for producing one ammonia molecule ($n = 3$), F is the Faraday constant ($F = 96\,485.33$ C mol^{-1}), C is the concentration of ammonia formed in the reaction, V is the volume of electrolyte in the electrochemical cell, M is the molar mass of ammonia ($M = 17$ amu), and Q is the total charge passed through the system.

UHV-EC Methods. UHV-EC studies were carried out in a separate XPS system with attached electrochemical cell as described previously.[11] Briefly, the sample was transported to proximity with the electrochemical cell to place the electrolyte meniscus in contact with the sample surface. Withdrawal of the sample from the electrolyte was followed by sample rinsing in DI water, then pump-down of the transfer chamber, and sample transfer to the XPS analysis chamber, which had a base pressure of 3×10^{-9} Torr. The analysis chamber was equipped with a 140 mm mean radius hemispherical analyzer (Physical Electronics) equipped with a microchannel plate detector and Omnifocus lens. XPS spectra were acquired in constant pass energy mode (23.5 eV) in either normal or grazing emission mode (see above) using unmonochromatized Al Kα radiation. XPS spectral analysis was carried out as described above but using atomic sensitivity factors appropriate to this analyzer.[35]

Computational Methods. Plane-wave DFT computations utilized the VASP package version 5.4.4.[36] van der Waals and continuum solvation corrections were included in the reported simulations.[37] Calculations utilized a plane wave cutoff energy of 500 eV; SCF convergence was considered to be $<1 \times 10^{-5}$ eV. Surface calculations were done in an asymmetrical unit cell of $a = b = 8.79$ Å, $c = 33.16$ Å, $\alpha = \beta = \gamma = 90°$ and used a K-point mesh of $3 \times 3 \times 1$. Calculations utilized first-order Methfessel−Paxton smearing with $\sigma = 0.2$ eV.[38]

Simulations utilized spin-polarized methods, with projector-augmented wave potentials and GGA functionals.[37] The DFT-D3 van der Waals correction[39] with Becke−Johnson[40] damping was included in the simulations.

RESULTS AND DISCUSSION

Characterization of Deposited Films. *XRD.* The crystalline phases of NbC and TaC films after deposition were studied by *ex situ* X-ray diffraction (XRD), and the results are shown in Figure 1. Results for the NbC film (Figure 1a) indicate that the niobium carbide film is polycrystalline with cubic rock salt structure. The XRD spectra show NbC diffraction peaks with different orientations: NbC (111) (PDF no. 01-074-1222) and NbC (311) (PDF no. 01-074-1222). Other XRD diffraction peaks present in the spectra are associated with niobium oxide species including Nb_2O_5 (−610) (PDF no. 00-037-1468), Nb_2O_5 (−818) (PDF no. 00-037-1468), $NbO_{0.8}$ (220) (PDF no. 04-008-0300), and Nb_2O_5 (4010) (PDF no. 00-037-1468).

Figure 1b shows the XRD results for the polycrystalline TaC film. The major diffraction peaks correspond to TaC (111), TaC (200), TaC (220), TaC (311), and TaC (222) planes for a NaCl-type crystalline structure. The results indicate that the deposited TaC film exhibits a cubic crystal structure (PDF no. 00-035-0801). No evidence of tantalum oxide diffraction peaks is present. This indicates that oxide phases are either not present in bulk and only present as thin surface films not observable by XRD, or else are present in the bulk only as amorphous phases. The XPS results (but see below) support the former explanation.

SEM/EDX. The above explanation is further corroborated by SEM data for deposited NbC (Figure S2) and TaC films (Figure S3). The SEM/EDX data in general show a uniform

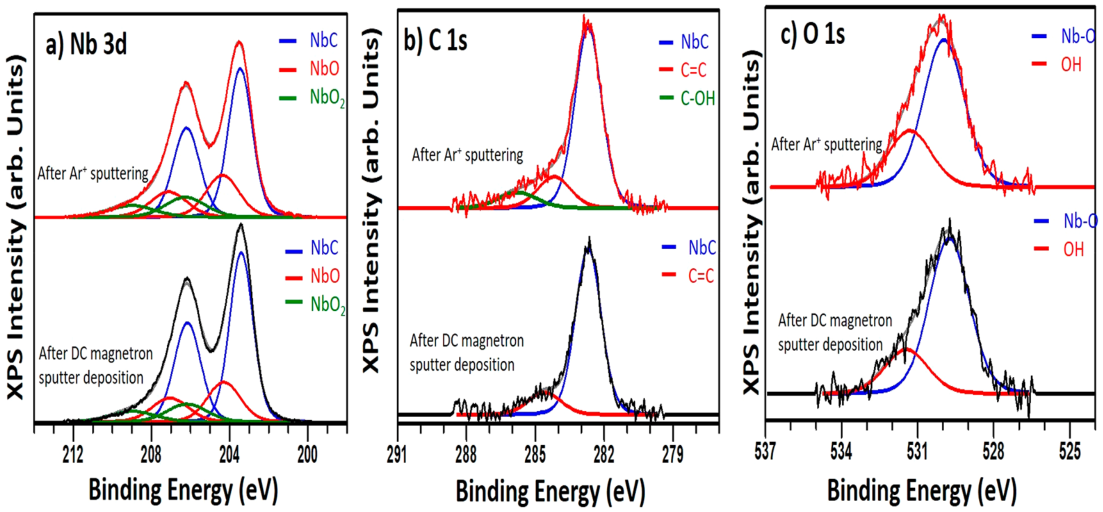

Figure 2. Core-level XPS spectra of NbC after 30 min of DC magnetron sputter deposition at 30 W, 8 mTorr of Ar, and 800 K (black spectra) and after 30 min of Ar$^+$ sputtering at 3 keV (red spectra): (a) Nb 3d, (b) C 1s, and (c) O 1s for NbC. Spectra were acquired at normal emission.

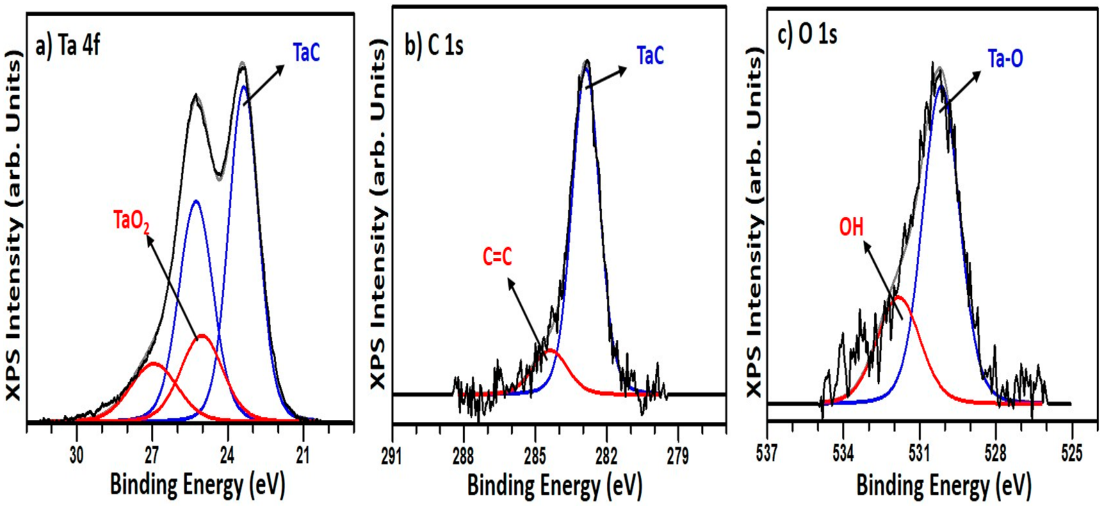

Figure 3. Core-level XPS spectra of TaC after deposition: (a) Ta 4f, (b) C 1s, and (c) O 1s for TaC. Spectra were acquired at normal emission. No sputtering was required to remove metallic phases.

distribution of the metal, carbon, and Sn from the FTO substrate. An important difference, however, is the presence of multiple concentrated O spots in the NbC films (Figure S2d) but not in the corresponding TaC film (Figure S3d) These results demonstrate that the absence of Ta oxide phases in the TaC XRD spectrum (Figure 2b) indicates the absence of such phases (either polycrystalline or amorphous) in the bulk of the TaC film.

In Situ XPS. XPS spectra (normal emission) before/after Ar$^+$ ion sputtering (of NbC) to achieve a stoichiometric Nb:C phase are displayed in Figure 2. The data demonstrate that the Ar$^+$ sputtering (30 min at 3 keV) induced only minor changes in the Nb 3d, O 1s, and C 1s core level spectra. Corresponding *in situ* TaC data (acquired without preliminary sputtering), are displayed in Figure 3.

The data in Figures 2 and 3 demonstrate that both films are predominantly metal carbide in nature (in agreement with the XRD data, Figure 1) but with significant Nb oxide (Figure 2) and Ta oxide (Figure 3) phases apparent. The XRD data in Figure 1 suggest that Nb oxide phases are distributed at both the surface and subsurface regions, whereas only surface oxide layers are found for TaC (Figure 3). To resolve this issue, grazing emission core level XPS spectra were acquired for the NbC film shown in Figure 2. The normal and grazing emission XPS spectra are compared in Figure 4. Corresponding TaC data are compared in Figure 5.

Notably, the data in Figures 2 and 4 show that Nb oxide phases are present in similar relative intensities in both normal and grazing emission, indicating the presence of these oxides at both the surface and subsurface regions, consistent with the XRD and SEM data (Figures 1 and S2.) However, corresponding data for TaC (Figures 3 and 5) indicate a much greater relative intensity for Ta oxide in grazing emission, indicating that such oxides are present primarily at the surface of the film but not so in the subsurface region, again consistent with XRD (Figure 1) and SEM data (Figure 2).

The data in Figures 1−5 demonstrate that DC magnetron sputter deposition of a NbC film, even after brief Ar ion sputtering to remove surface metal phases, yields a film with Nb oxides present at both the surface and in the bulk. In contrast, the corresponding data for TaC films deposited under

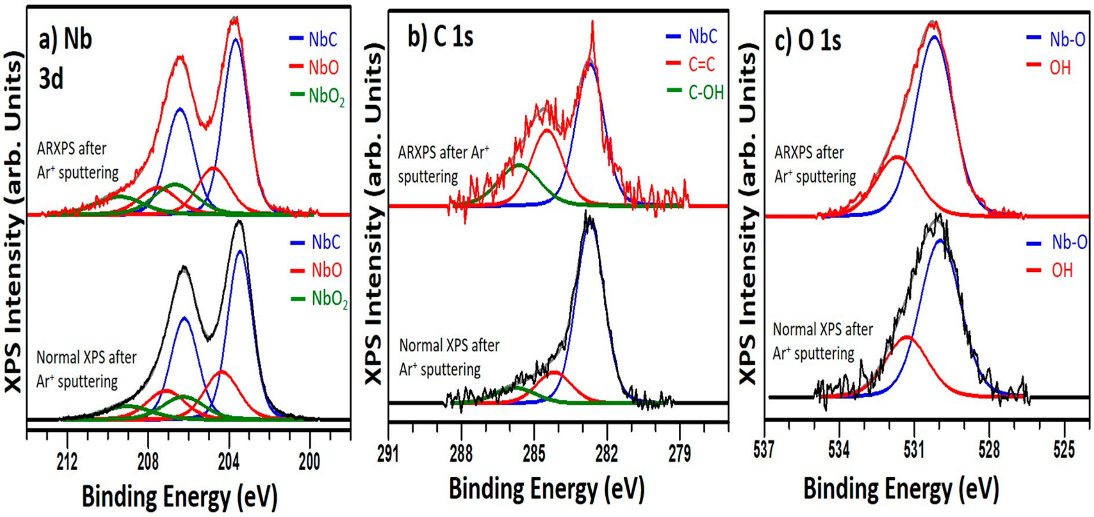

Figure 4. XPS grazing (red, upper trace) vs normal emission (black, lower trace) for NbC film after Ar ion sputtering: (a−c, top) Nb 3d, C 1s, and O 1s spectra, respectively, acquired at grazing emission; (a−c, bottom) corresponding spectra acquired at normal emission. Same film as in Figure 2.

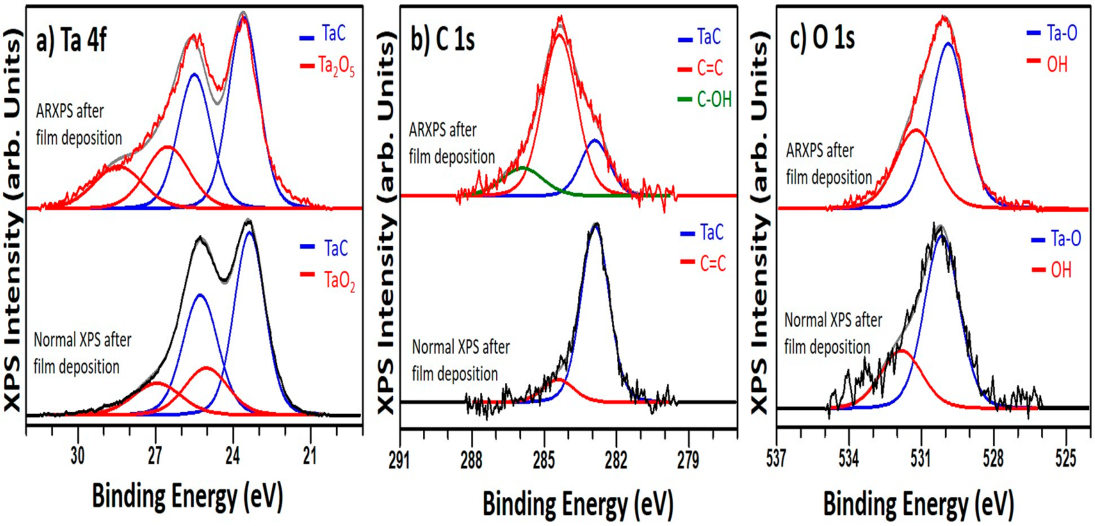

Figure 5. XPS grazing (red, upper trace) vs normal emission (black, lower trace) for TaC film after Ar ion sputtering: (a−c, top) Ta 4f, C 1s, and O 1s spectra, respectively, acquired at grazing emission; (a−c, bottom) corresponding spectra acquired at normal emission. Same film as in Figure 3.

very similar conditions indicate the presence of some Ta oxide phases predominantly at the surface and not in the bulk. However, such phases are present even after brief Ar^+ sputtering.

Additionally, the grazing emission XPS data (Figures 4 and 5) show that both NbC and TaC films, even in the absence of ambient exposure, exhibit significant thicknesses of adventitious and (possibly) other noncarbidic C phases at binding energies in excess of ∼283 eV. For NbC, identifying the C 1s spectrum acquired at grazing emission (Figure 4) as composed of a carbidic carbon phase with a peak maximum at 282.7 eV,[22,23] a broad graphitic carbon feature near 284.2 eV,[4,22,41,42] and a C−OH feature, apparent only after Ar^+ sputtering at 285.8 eV[22,41,43,44] yields an estimated thickness of the noncarbidic carbon overlayer of ∼5.8 Å. Quantitative analysis of the niobium carbide Nb $3d_{5/2}$ (∼203.5 eV) and C 1s (∼282.7 eV) peaks yielded an Nb:C atomic ratio of 1.00:0.99, indicating the formation of a stoichiometric NbC phase. The spectra in the O 1s region, Figure 3c, were fitted with two components arising from Nb−O bonds at 530.0 eV[22,28,43] and hydroxyl groups at 531.3 eV.[4,43−47]

A similar analysis of the TaC core level spectra acquired at grazing emission (Figure 5) indicates the presence of multiple Ta oxidation states associated with TaC at binding energies of 23.4 eV [$4f_{7/2}$] and 25.3 eV [$4f_{5/2}$][25,48,49] and TaO_2 centered at 25.0 [$4f_{7/2}$] eV and 26.9 eV[$4f_{5/2}$].[50] The C 1s spectra in Figure 5b were deconvoluted into two components at 282.9 and 284.4 eV, which correspond to TaC[24,25] and graphitic C (sp^2-C),[4,22,41,42] respectively. The presence of graphitic carbon in the film results from sample preparation. XPS analysis reveals that the thickness of the graphitic C overlayer is ∼4.5 Å. In contrast to NbC, there is no evidence (Figure 4b) for oxidized or hydroxylated C in the deposited film.

Thus, the XPS data (Figures 4 and 5) demonstrate that surface oxides and noncarbidic carbon phases are present for both films, even though deposition was carried out in a chamber with a base pressure of $<1 \times 10^{-8}$ Torr. In the case of NbC, the noncarbidic carbon phase was not readily removed

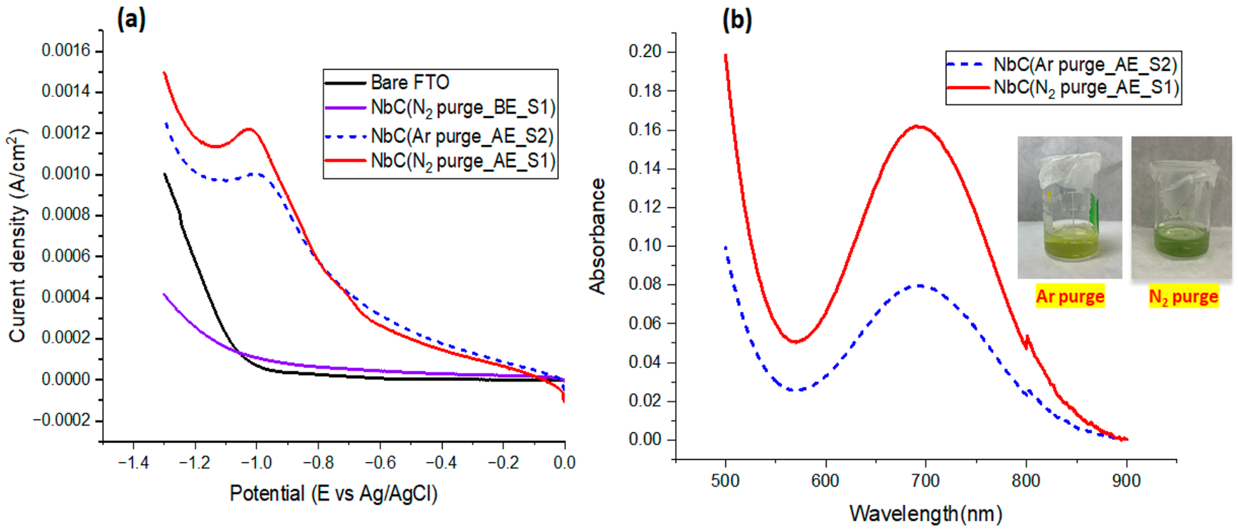

Figure 6. Electrochemical measurements on NbC films immersed in 0.3 M NaOH prior to measurements in 0.1 M Na_2SO_4 solution adjusted to pH 3.2 with sulfuric acid. (a) LSVs of NbC in solution: (red) sample 1, NaOH-treated, N_2-purged solution; (purple) sample 1, untreated, N_2-purged solution; (black) bare FTO, N_2-purged solution; (blue-dashed) sample 2, NaOH-treated, Ar-purged solution. (b) Absorption measurements for indophenol blue after 1 h of electrolysis at −1.0 V vs Ag/AgCl for 1 h; (blue-dashed), Sample 2, NaOH-immersed, Ar-purged solution; (red) Sample 1, NaOH-immersed, N_2-purged solution. The blue-dashed absorption curve in (b) is at background for this spectrometer and measurement (see beakers, inset).

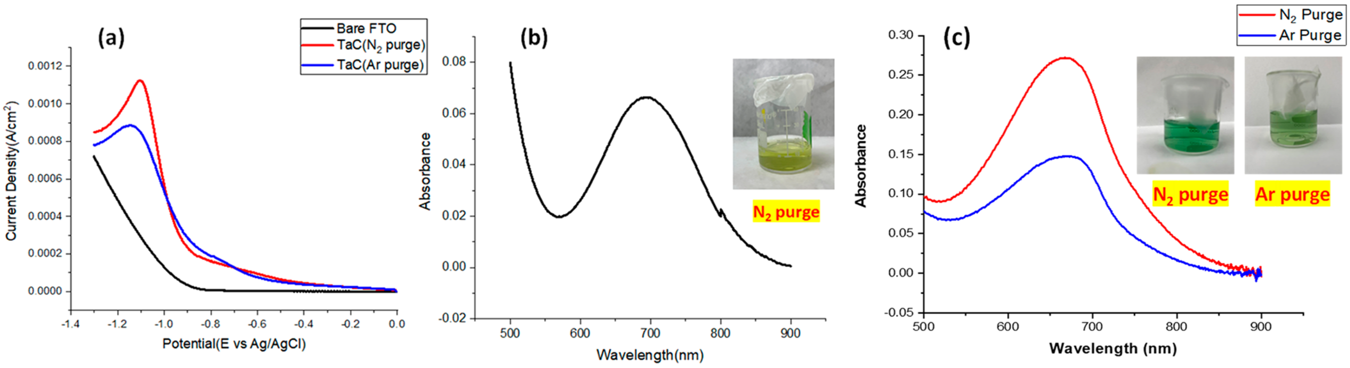

Figure 7. Electrochemical measurements on a TaC film immersed in 0.3 M NaOH prior to measurements in 0.1 M Na_2SO_4 solution adjusted to pH 3.2. (a) LSVs of NaOH-treated TaC in solution: (red) N_2-pured; (blue) Ar-purged; (black) bare FTO. (b) Absorption measurements for indophenol blue after 1 h of electrolysis in N_2-purged solution at −1.0 V vs Ag/AgCl for 1 h. The absorbance shown is at the level of background, indicating no NH_3 formation. (c) Absorption measurements for indophenol blue after 1 h of electrolysis in N_2-purged solution (red) and Ar-purged solution (blue) at −1.15 V vs Ag/AgCl for 1.5 h.

by Ar^+ sputtering. The significant presence of surface oxides and noncarbidic carbon (and, in the case of NbC, bulk oxide phases) even in a system with rigorous control of the base and operating pressures indicates that such “imperfections” must be accounted for when considering the surface reactivities of these materials.

Electrochemical Studies. NbC stoichiometric films >180 Å thick, deposited on FTO substrates, were tested for NRR activity both without and with preliminary 0.3 M NaOH immersion/rinsing. Measurements of both treated and untreated NbC and TaC films were carried out in a 0.1 M Na_2SO_4 solution adjusted to pH 3.2 with sulfuric acid.

Linear scan voltammograms (LSVs) for NaOH-treated and untreated NbC films in N_2-purged electrolyte solution are displayed in Figure 6a. These data are compared in Figure 6a to an LSV for a second, identically prepared and NaOH-treated NbC film in Ar-saturated electrolyte. Corresponding indophenol blue absorption measurements are displayed in Figure 6b for NaOH-treated films in both Ar-purged and N_2-purged solutions. The data in Figure 6a show that at cathodic potentials more positive than approximately −1.0 V vs Ag/AgCl, the response of the untreated NbC film in an N_2-purged solution (blue trace) is similar to that of a bare FTO surface (black trace). In contrast, NaOH-treated NbC in N_2-purged solution (red trace) exhibits markedly enhanced current at potentials more positive than approximately −1.0 V, indicating significant NRR activity. The LSVs of NaOH-treated NbC films in both Ar-purged (blue-dashed line) and N_2-purged (red line) solutions (Figure 6a) indicate significant electrochemical activity for treated NbC even in the absence of N_2.

That NaOH-treated NbC is NRR active, however, is demonstrated by the corresponding absorption spectra (Figure 6b) for a treated film in an N_2-saturated solution (red trace) and for a second treated NbC film in Ar-saturated solution (blue-dashed trace). The intensity of the blue-dashed trace is at the background for this spectrometer, while the magnitude for the red trace shows significant NH_3 production (FE ∼ 3.15%) at −1.0 V vs Ag/AgCl for 90 min. In summary, the data

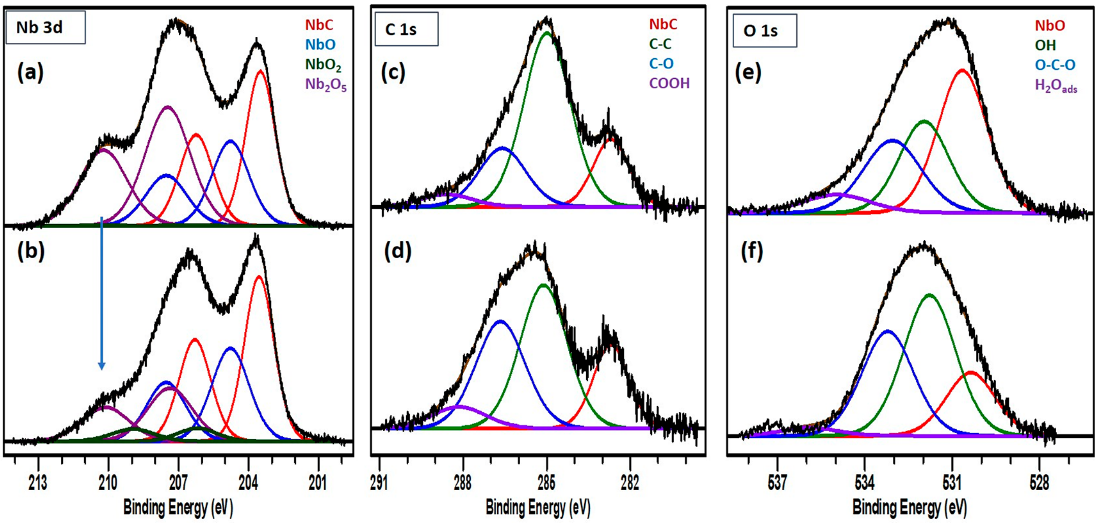

Figure 8. XPS core level spectra of NbC: (a) N 3d XPS spectra prior to NaOH treatment; (b) Nb 3d XPS spectra after NaOH treatment, immersion in 0.1 M Na_2SO_4 adjusted to pH 3.2 at open circuit potential, emersion, and rinsing in DI H_2O; (c, d) corresponding data for C 1s; (e, f) corresponding data for O 1s. All spectra were acquired in grazing emission geometry. The arrow is a guide for the eye.

in Figure 6 demonstrate that at potentials more positive than −1.0 V Ag/AgCl, NaOH-treated NbC is NRR active, while untreated NbC is electrochemically very similar to the FTO substrate. The FE of 3.15%, although relatively small compared to many reports in the literature,[15] is substantial in comparison with results for other thin films with relatively low surface areas.[19]

Corresponding data for similarly treated TaC are displayed in Figure 7, upon immersion in Ar-purged (blue) and N_2-purged electrolytes (red). The LSVs (Figure 7a) show that the presence of N_2 induces little significant additional cathodic current at potentials below approximately −1.0 V vs Ag/AgCl, indicating negligible NRR activity in this range. This conclusion is corroborated by the absorbance data (Figure 7b) (acquired at −1.0 V vs Ag/AgCl for 90 min) indicating no absorbance above the background (e.g., the blue dashed curve in Figure 6b). However, the data in Figure 7c show that polarization in N_2-purged solution to a slightly more negative potential (−1.15 V vs Ag/AgCl) does yield observable NH_3 formation, albeit at a very small FE of 0.21%. The data in Figure 7, therefore, demonstrate that TaC, even after immersion in 0.3 M NaOH and subsequent rinsing, is NRR inactive at potentials more positive than −1.0 V vs Ag/AgCl while exhibiting a minor degree of NRR activity at more negative potentials. The data in Figure 7a, however, demonstrate that NaOH-treated TaC, in both Ar-purged and N_2-purged solutions, exhibits significantly higher cathodic current than bare FTO at all potentials of <−1.0 V vs Ag/AgCl.

The data in Figures 6a and 7a demonstrate that significant electrochemical reactions are occurring for NaOH-treated NbC and TaC, even in the absence of N_2. A number of such reactions, including HER, are of course possible. Understanding this phenomenon could be of importance in understanding catalytic efficiency as related to surface composition and will require further investigation.

UHV-EC Results. The NbC XPS core level spectra of the ambient-exposed NbC sample before and after immersion/emersion in 0.3 M NaOH at open circuit potential (OCP) and subsequent rinsing in DI water are displayed in Figure 8. Studies at OCP were designed to replicate the procedures used in the electrochemical experiments, with (i) sample immersion in 0.3 M NaOH, (ii) brief rinsing in DI water, (iii) immersion in the electrolyte at OCP, and (iv) emersion, rinsing in DI water and transfer for XPS analysis of the surface. All spectra shown in Figure 8 were acquired in grazing emission geometry to emphasize sensitivity to NbC oxide surface overlayers as opposed to near-surface inclusions (e.g., Figure 1a).

Nb 3d spectra (Figure 8a,b) demonstrate that the NaOH immersion/rinsing process substantially reduces the Nb_2O_5 overlayer induced by ambient exposure. Calculations of Nb_2O_5 average thickness before/after NaOH treatment indicate corresponding average thicknesses of ∼9 and 4 Å, respectively. Such figures should be regarded with caution, however, as even in grazing emission geometry, some subsurface oxides may still be observed, and the exact effects of brief sample exposure to H_2O vapor before/after sample transfer cannot be ignored. Indeed, experiments in which a Nb_2O_5/Nb suboxide/Nb metal sample was exposed to H_2O vapor over the electrochemical cell, but not to liquid electrolyte (to mimic the transfer process), yielded an observable increase in the Nb_2O_5 average thickness, from ∼39 Å to 44 Å. (See Figure S4, Supporting Information.) Therefore, the finding of an average Nb_2O_5 film thickness of ∼4 Å after the NaOH treatment process (Figure 8) must be regarded as an "upper bound" for the amount of Nb_2O_5 actually present.

Corresponding C 1s spectra (Figure 8c,d) exhibit a substantial adventitious C component near 285.0 eV binding energy,[41] an increase in a feature attributable to C−OH species near 286.0 eV binding energy,[22,41,44] and a component at higher binding energies tentatively attributed to COOH species.[22,41,44] The C 1s spectra indicate that the NbC surface (as treated in the NbC electrochemistry studies) contains substantial noncarbidic surface carbon both before and after the immersion/emersion process. Estimates of the average thickness of the noncarbidic carbon surface layer average thickness before and after NaOH treatment are 8.7 and 4.1 Å, respectively. This indicates that the sample, unsurprisingly, contains substantial adventitious and hydroxylated C at the surface, with the latter substantially increased after the

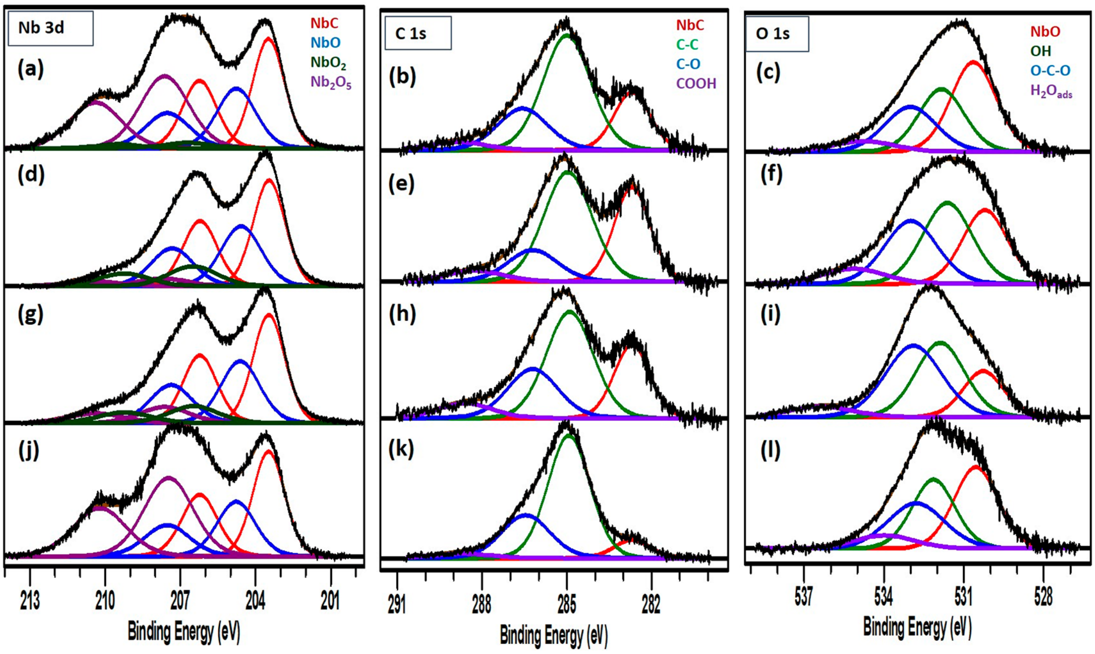

Figure 9. Evolution of NbC core level XPS spectra as a function of applied cathodic potential. All spectra were acquired in normal emission geometry. (a) Nb 3d, (b) C 1s, and (c) O 1s XPS spectra of NbC after ambient exposure but before NaOH treatment (same sample as in Figure 8a,c,e). Corresponding spectra after NaOH treatment and immersion/emersion at OCP in 0.1 M Na_2SO_4 adjusted to pH 3.2 are shown in (d)−(f), respectively (same sample as Figure 8b,d,f.). Corresponding spectra after immersion and polarization to −1.0 V vs Ag/AgCl are shown in (g)−(i). Corresponding spectra after immersion and polarization to −1.3 V vs Ag/AgCl are shown in (j)−(l).

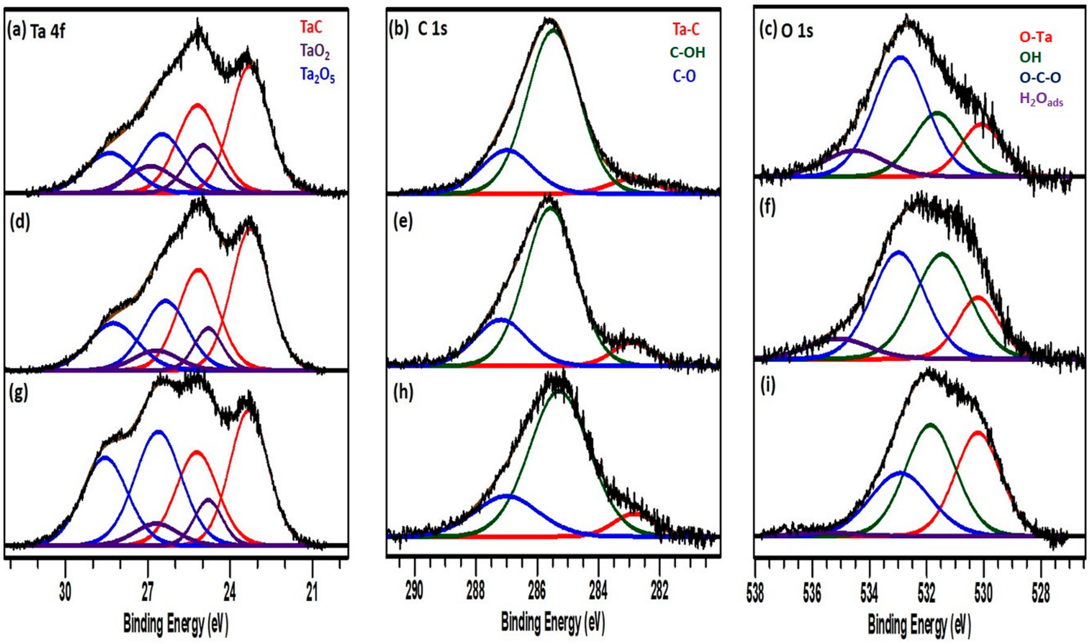

Figure 10. TaC XPS core level spectra as a function UHV-EC experiments, where all spectra were acquired in normal emission geometry: (a−c) Ta 4f, C 1s, and O 1s XPS spectra after ambient exposure but before NaOH treatment, (d−f) after NaOH treatment, and (g−i) after immersion in electrolyte and polarization to −1.0 V vs Ag/AgCl.

immersion/emersion process. O 1s spectra (Figure 8e,f) indicate substantial amounts of molecularly adsorbed H_2O before the process (Figure 8e), and significant coverage with OH groups bound to carbon after the process (Figure 8f). In summary, the data of Figure 8 demonstrate that preliminary immersion in NaOH removes most (if not all) Nb_2O_5 from the surface region and also show that significant thicknesses of adventitious C are present at the surface but do not inhibit the NRR activity of the partially oxidized NbC surface.

The evolution of NbC core level spectra as a function of polarization to different cathodic potentials is displayed in Figure 9. (All spectra were acquired in normal emission geometry.) Spectra in Figure 9a−c were acquired on the same sample as in Figure 8a,c,e. Spectra in Figure 9d−f were acquired on the same sample as in Figure 8b,d,f. These spectra

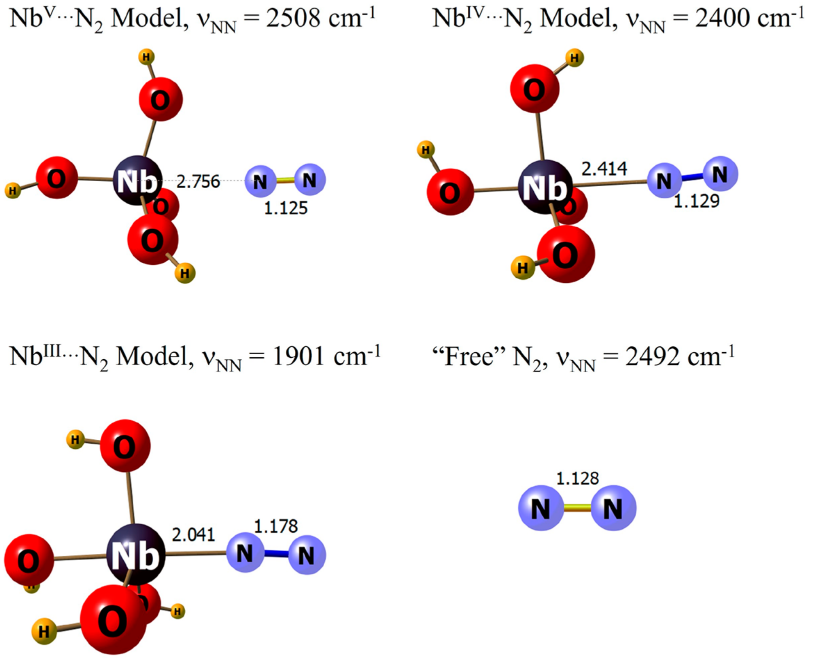

Figure 11. DFT optimized molecular geometries for N_2–Nb($+x$) binding models for x = 5, 4, 3, and “free” dinitrogen (lower right). Bond lengths are in angstrom units.

show (as in Figure 8) that immersion in NaOH, followed by rinsing in DI water and immersion/emersion at OCP, yields a surface with the Nb_2O_5 surface layer largely removed and with a significant surface coverage of noncarbidic, partially hydroxylated C. Subsequent immersion and polarization to −1.0 V vs Ag/AgCl (Figure 9g−i) yield little observable change in the Nb 3d or C 1s spectra but some shift in the O 1s spectrum (Figure 9i) toward higher binding energies, possibly associated with enhanced oxidation/hydroxylation of surface C species. Polarization to −1.3 V vs Ag/AgCl (Figures 9j−l) did, however, indicate significant surface changes corresponding to the peaks and subsequent decrease in the cathodic current (Figure 6a). The Nb 3d spectrum (Figure 9j) indicates that polarization to this potential induces regrowth of a Nb_2O_5 surface layer. Changes in the C 1s spectrum (Figure 9k) correspond to a significant decrease in the relative intensity of the carbidic carbon feature near 282.7 eV binding energy.

The XPS data in Figure 9 in concert with the electrochemistry results (Figure 6a) indicate that the NbC surface composition is relatively stable to approximately −1.0 V vs AgCl but that polarization to more cathodic potentials results in a reoxidation of the surface, in concert with a reaction that decreases the amount of carbidic C in the surface region, possibly due to the oxidation/dissolution of C at surface carbide sites.

Data in Figure 10 demonstrate that, in contrast to NbC, immersion of the ambient-exposed TaC sample (Figure 10a−c) in 0.3 M NaOH followed by rinsing in DI water and subsequent immersion/emersion at OCP does not result in removal of a Ta_2O_5 surface layer (Figure 10d−f). However, the polarization of the TaC surface to −1.0 V vs Ag/AgCl does yield enhanced oxidation of the surface by increasing the thickness of the Ta_2O_5 layer, as shown in Figure 10g−i.

In summary, the experimental data in Figures 1−10 demonstrate that (a) immersion of ambient-exposed NbC in 0.3 M NaOH prior to electrocatalysis yields an NRR active electrode surface at cathodic potentials more positive than −1.0 V vs Ag/AgCl, correlated with removal of all or most of the ambient-induced Nb_2O_5 surface layer (Figures 6 and 8), and that polarization to larger cathodic potentials induces an increase and subsequent decrease in cathodic current correlated with surface reoxidation (Figure 9). In contrast, similar treatment of ambient-exposed TaC does not remove the Ta_2O_5 surface layer, and this is correlated with NRR inactivity at cathodic potentials more positive than −1.0 V vs Ag/AgCl, although other electrochemical reactions appear to occur (Figures 7 and 10). As with NbC, however, the polarization of TaC to higher cathodic potentials does induce a peak in current corresponding to enhanced surface oxidation (Figures 7 and 10), and electrolysis measurements at −1.15 V vs Ag/AgCl indeed indicate a low rate of NRR activity: 0.21% FE vs 3.15% FE for NaOH-treated NbC at −1.0 V (Figure 7c).

These data (both the sharp maxima in cathodic currents for both carbides at highly negative potentials and the slight NRR activity observed for TaC) suggest the occurrence of hydrolysis. In such a process, the splitting of a water molecule would yield both surface hydroxylation (yielding Nb^{V}, as in Figure 9j) and protons for reaction with N_2. This, however, cannot be definitively concluded from the existing data, and further experiments are necessary.

DFT Results. The experimental data demonstrate that NbC NRR activity, as shown in Figure 6, is correlated with the presence of surface Nb sites in intermediate oxidation states (i.e., +4 or +3, rather than +5), as indicated by changes in the Nb 3d XPS spectrum (Figure 8a,b) due to sample pretreatment with NaOH, which greatly reduces the Nb^{5+} component of the Nb 3d spectrum. Previous calculations[14,15,19] demonstrate that such intermediate oxidation states are much more effective than Nb^{V} in activating $N\equiv N$ bonds, illustrating the importance of π-backbonding for NRR. What needs to be addressed, however, is whether Nb ions with intermediate oxidation states are more effective than Nb^{V} in binding N_2 in aqueous solution. To address this issue, DFT-based calculations (plane-wave (surface models) and atom-centered (molecular models)) were carried out using $Nb(OH)_4$ clusters for the latter as shown in Figure S5 (Supporting Information). The overall charge of the molecular model was adjusted to modulate the formal oxidation state of the Nb using typical counting rules, i.e., hydroxide is formally a 1− charge. Molecular calculations accounted for the effects of solvation via a continuum model[51] (SMD) without trying to specifically account for the undoubtedly complex nature of the various oxide surface structures. Additionally, calculations of binding energy accounted for the exchange of N_2 (bonded end on) with a previously bound water molecule (bound via the O lone pair) according to the reaction

$$^{*}H_2O + N_2 \rightarrow {}^{*}N_2 + H_2O$$

where * represents the Nb cation site with a specific formal oxidation state.

Results for the molecular calculations (Gaussian 16, PBE0 functional, CEP pseudopotentials; see Supporting Information for additional details) are summarized in Figure 11. The DFT results, consistent with experiment, show that N_2 does not bind and is not activated at Nb^{V} sites: r_{NbN} = 2.756 Å, r_{NN} = 1.125 Å, ν_{NN} = 2505 cm^{-1}), cf. dinitrogen, which has r_{NN} = 1.128 Å and ν_{NN} = 2492 cm^{-1} at the same level of theory. To corroborate these molecular results for solid-state models, $^{*}N_2$ was optimized using plane-wave DFT for the 001 face of Nb_2O_5 ($C2/m$ space group, which is the lowest energy polymorph in the Materials Project database). Upon optimization of this surface model with plane-wave DFT (Figure 12), the N_2 is only very tenuously bonded, r_{NbN} = 2.543 Å, r_{NN} = 1.108 Å, akin to what was seen with the molecular $Nb(OH)_4$ models.

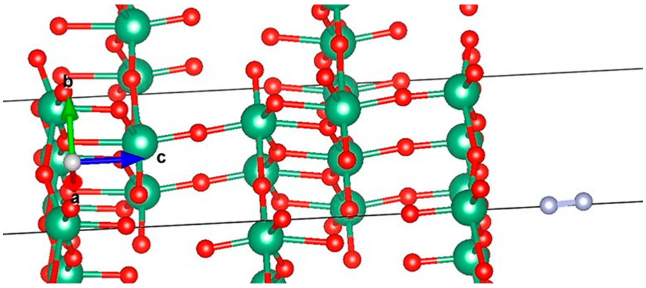

Figure 12. Optimized $^{*}N_2$ for $C2/m$-$Nb_2O_5(001)$ surface: end-on very weak coordination of N_2 (gray spheres) to a surface Nb^{V} cation (green spheres); O atoms are red spheres. The c axis is marked in blue. r_{NbN} = 2.543 Å, r_{NN} = 1.108 Å.

Furthermore, calculated N_2 activation upon binding to niobium (as evidenced by lengthened NN bond lengths and a diminution of the NN stretching frequencies upon metal coordination) is more significant for Nb^{III} than for Nb^{IV} molecular models (e.g., r_{NbN} = 2.041 Å, r_{NN} = 1.178 Å, ν_{NN} = 1901 cm^{-1} for Nb^{III} and r_{NbN} = 2.414 Å, r_{NN} = 1.129 Å, ν_{NN} = 2400 cm^{-1} for Nb^{IV} models).[19] Thus, the data in Figure 11, together with previous calculations[19] and the experimental data described above, demonstrate that π-backbonding between the transition metal site and N_2 is critically important not only for N≡N bond activation but also in N_2-surface binding.

In a previous study by our group, room temperature ambient pressure XPS experiments with N_2 and H_2O partial pressures of ∼0.5×10^{-1} Torr each[12] indicate that N_2/OH_2 binding at V oxide surface sites is competitive. Corroborating DFT calculations of different V oxide surfaces suggest that the binding of N_2 and OH_2 changes in response to the formal oxidation state of the metal ions.[12] More positive formal oxidation states favor the binding of the σ-donor water ligand, while lower metal formal oxidation states favor N_2 binding due to enhanced π-backbonding. To this end, the OH_2/N_2 reaction energy as calculated, per the above exchange reaction, for the Nb^{III} and Nb^{IV} models, Figure S5. N_2 dissociates from Nb^{V} upon geometry optimization, precluding this energy calculation for the d^0 state of niobium. For the Nb^{IV} models, the exchange reaction is computed to be endergonic, i.e., water binding is preferred over dinitrogen binding, ΔG = +11.8 kcal/mol. However, upon reducing the niobium to 3+, the exchange is now computed to be exergonic, ΔG = −18.1 kcal, indicating that N_2 is now preferentially bound. Given the simple models used (Figure S5), the precision of such values must be regarded with caution. The trend, however, strongly suggests that competitive binding of N_2 versus H_2O at the metal cation site may play a role in selectivity for NRR versus HER.

Also, an issue is the different behaviors of NbC and TaC toward metal oxide formation during sputter deposition (e.g., Figures 1 and 2). These experimental data suggest that not only oxophilicity, but carbophilicity (the strength of metal−carbon bonds) is important for the speciation of the carbide surfaces under catalytic conditions. Plane-wave DFT calculations were therefore performed to assess the formation energies of rs-NbC_xO_y and rs-TaC_xO_y as a function of the C/O ratio to probe the subtle differences in carbophilicity and oxophilicity of these two metals (rs = rock salt). For simplicity, and to examine the role of metal−oxygen vs metal−carbon bond strengths, calculations assumed rock salt structures for all carbides, oxides, and oxycarbides. Results are displayed in Figure S6.

The data in Figure S6 indicate that Nb oxides have larger energies of formation than corresponding Ta oxides, while Ta carbides are more stable than corresponding Nb carbides. These results are indicative of slightly greater Ta carbophilicity versus Nb coupled with slightly greater oxophilicity for Nb versus Ta and explain the formation of both Nb oxides and carbide phases during carbide sputter deposition, whereas TaC phases were deposited without nonsurface oxide phases (Figures 1 and 2).

■ SUMMARY AND CONCLUSIONS

Experimental XRD, SEM, and *in situ* photoemission data (Figures 1, 2, and 4 and Figures S2 and S3) demonstrate that NbC and TaC films prepared by DC magnetron sputter deposition at base pressures of <10^{-8} Torr exhibit important differences, including the presence of oxide phases throughout the NbC film, but only at the surface of the TaC film. Preliminary immersion in 0.3 M NaOH and then rinsing, prior to electrochemistry, produce a NbC sample that is active for NRR at pH 3.2 (Figure 6), with a FE of >3%, which is quite significant for a sputter-deposited thin film surface.[52,53] UHV-EC results (Figures 8 and 9) correlate NbC NRR activity with the removal of much, if not all Nb_2O_5 at the solid/electrolyte interface. A decrease in NRR activity at potentials more negative than ∼1.0 V vs Ag/AgCl (Figure 6) is correlated with a re-formation of the Nb_2O_5 surface layer at more cathodic potentials (Figure 9).

TaC, in contrast, exhibits an ambient-induced Ta_2O_5 surface layer, even after similar NaOH treatment. This sample is NRR inactive at potentials more positive than −1.0 V vs Ag/AgCl

(Figure 7a,b). At −1.15 V vs Ag/AgCl, however, some NRR activity is observed (Figure 7c), though the FE of 0.21% is more than an order of magnitude below that observed for the NbC sample.

The unusual phenomena observed for both samples at potentials more negative than −1.0 V vs Ag/AgCl (pronounced maxima in the cathodic current, reoxidation of the NaOH-reduced Nb suboxide surface layer, and some NRR activity in the TaC sample) suggest an unusual phenomenon, such as hydrolysis. Such phenomena (surface oxidation under cathodic conditions) are well-known and have been reviewed in the literature.[54] A definite conclusion on this issue, however, will require additional study.

DFT calculations of Nb oxide/N_2 surface interactions, considering the presence of H_2O, corroborate the experiment in indicating very weak interactions between N_2 and Nb^{V} oxide but stronger interactions between N_2 and Nb^{IV} or Nb^{III} oxides (Figures 11 and 12). Indeed, the theoretical results suggest that N_2 will displace adsorbed H_2O from Nb^{III} centers but not from Nb^{IV}. This result is similar to experimental and theoretical findings for V oxides, based on NAP-XPS, UHV-EC, and theoretical work.[12] While this would explain the NRR activity of the NaOH-treated NbC sample at pH 3.2, the complexity of the corresponding XPS spectra does not allow us to decisively conclude, at this time, that Nb^{III} oxide is the NRR-active surface under the conditions examined.

The results for TaC are in sharp contrast to those for NbC. Ta oxide phases are found only at the surface of the sputter-deposited surface (Figures 1−4). After NaOH treatment identical to that done to the NbC sample, the TaC sample displays very little NRR activity at pH 3.2, although significant, similar cathodic currents are observed in both Ar-saturated and N_2-saturated solutions (Figure 7). The electrochemical behavior of the NaOH-treated TaC sample is correlated with the stability of the surface Ta_2O_5 surface layer in the face of immersion in NaOH (Figure 10). The different behaviors of the TaC and NbC surfaces during deposition, immersion in NaOH solution, and electrochemical testing cannot be entirely explained by the above data, as both Ta and Nb are highly oxophilic.[13] However, DFT calculations suggest that at least part of the reason is stronger Ta−C bond strength (Figure S6), i.e., greater carbophilicity[55] of Ta versus Nb.

In conclusion, experimental and theoretical results demonstrate that ambient-exposed NbC, upon immersion in 0.3 MNaOH[9] and subsequent rinsing in DI water prior to immersion in the electrolyte at pH 3.2, yields Nb oxides in intermediate oxidation states (less than +5) that are highly active for NRR at cathodic potentials less than approximately −1.0 V vs Ag/AgCl. This high selectivity and activity are of course of practical as well as fundamental significance, and it remains to be determined whether the response of a Nb metal or oxide, under similar conditions, would differ from that of NbC. Such experiments are in progress in our laboratories.

■ ASSOCIATED CONTENT

Supporting Information

The Supporting Information is available free of charge at https://pubs.acs.org/doi/10.1021/acsami.3c11683.

Additional SEM and XPS data, plus additional computational data (PDF)

■ AUTHOR INFORMATION

Corresponding Author

Jeffry A. Kelber − *Department of Chemistry, University of North Texas, Denton, Texas 76203-5017, United States;* orcid.org/0000-0002-3259-9068; Email: Jeffry.kelber@unt.edu

Authors

Samar Alhowity − *Department of Chemistry, University of North Texas, Denton, Texas 76203-5017, United States*
Kabirat Balogun − *Department of Chemistry, University of North Texas, Denton, Texas 76203-5017, United States*
Ashwin Ganesan − *Department of Chemistry, University of North Texas, Denton, Texas 76203-5017, United States*
Colton J. Lund − *Department of Chemistry, University of North Texas, Denton, Texas 76203-5017, United States*
Olatomide Omolere − *Department of Chemistry, University of North Texas, Denton, Texas 76203-5017, United States*
Qasim Adesope − *Department of Chemistry, University of North Texas, Denton, Texas 76203-5017, United States*
Precious Chukwunenye − *Department of Chemistry, University of North Texas, Denton, Texas 76203-5017, United States*
Stella C. Amagbor − *Department of Chemistry, University of North Texas, Denton, Texas 76203-5017, United States*
Fatima Anwar − *Department of Chemistry, University of North Texas, Denton, Texas 76203-5017, United States*
M. K. Altafi − *Department of Chemistry, University of North Texas, Denton, Texas 76203-5017, United States*
Francis D'Souza − *Department of Chemistry, University of North Texas, Denton, Texas 76203-5017, United States*
Thomas R. Cundari − *Department of Chemistry, University of North Texas, Denton, Texas 76203-5017, United States;* orcid.org/0000-0003-1822-6473

Complete contact information is available at: https://pubs.acs.org/10.1021/acsami.3c11683

Author Contributions

[†]S.A. and K.B. contributed equally. The manuscript was written through the contributions of all authors. All authors have given approval to the final version of the manuscript.

Notes

The authors declare no competing financial interest.

■ ACKNOWLEDGMENTS

This work was supported by the U.S. National Science Foundation under Grant DMR-2112864, which is gratefully acknowledged. Additional NSF support for the UNT CASCaM HPC cluster via Grants CHE-1531468 and OAC-2117247 is also gratefully acknowledged. O.O. and S.A. also gratefully acknowledge partial support from the UNT College of Science. F.D. and T.R.C. acknowledge a seed grant for support of carbide studies from the UNT Division of Research & Innovation, Grant RSG-2023-002.

■ REFERENCES

(1) Humphreys, J.; Lan, R.; Tao, S. Development and Recent Progress on Ammonia Synthesis Catalysts for Haber-Bosch Process. *Adv. Energy Sustainability Res.* **2021**, *2*, 2000043.

(2) Qing, G.; Ghazfar, R.; Jackowski, S. T.; Habibzadeh, F.; Ashtiani, M. M.; Chen, C.; Smith, M. R. I., II; Hamann, T. W. Recent Advances and Challenges of Electrocatalytic N_2 Reduction to Ammonia. *Chem. Rev.* **2020**, *120*, 5437−5516.

(3) Hwu, H. H.; Chen, J. G. Surface Chemistry of Transition Metal Carbides. *Chem. Rev.* **2005**, *105*, 185−212.

(4) Wang, J.; Shen, L.; Ding, B.; Nie, P.; Deng, H.; Dou, H.; Zhang, X. Fabrication of Porous Carbon Spheres for High-performance Electrochemical Capacitors. *RSC Adv.* **2014**, *4*, 7538−7544.

(5) Kuang, M.; Huang, W.; Hegde, C.; Fang, W.; Tan, X.; Liu, C.; Ma, J.; Yan, Q. Interface Engineering in Transition Metal Carbides for Electrocatalytic Hydrogen Generation and Nitrogen Fixation. *Mater. Horiz.* **2020**, *7*, 32−53.

(6) Tafreshi, S. S.; Ranjbar, M.; Taghizade, N.; Panahi, S. F. K. S.; Jamaati, M.; de Leeuw, N. H. A First-Principles Study of CO_2 Hydrogenation on a Niobium-Terminated NbC (111) Surface. *ChemPhysChem* **2022**, *23*, No. e202100781.

(7) Ye, Y.; Xian, S.; Cui, H.; Tan, K.; Gong, L.; Liang, B.; Pham, T.; Pandey, H.; Krishna, R.; Lan, P. C.; Forrest, K. A.; Space, B.; Thonhauser, T.; Li, J.; Ma, S. Metal-Organic Framework Based Hydrogen-Bonding Nanotrap for Efficient Acetylene Storage and Separation. *J. Am. Chem. Soc.* **2022**, *144*, 1681−1689.

(8) Izelaar, B.; Ripepi, D.; Asperti, S.; Dugulan, A. I.; Hendrikx, R. W. A.; Böttger, A. J.; Mulder, F. M.; Kortlever, R. Revisiting the Electrochemical Nitrogen Reduction on Molybdenum and Iron Carbides: Promising Catalysts or False Positives? *ACS Catal.* **2023**, *13*, 1649−1661.

(9) Kimmel, Y. C.; Xu, X.; Yu, W.; Yang, X.; Chen, J. G. Trends in Electrochemical Stability of Transition Metal Carbides and Their Potential Use as Supports for Low-Cost Electrocatalysts. *ACS Catal.* **2014**, *4*, 1558−1562.

(10) Fang, D.; Wang, C.; Lv, C.; Lv, Y.; Huang, G.; Yang, J.; Pan, S. XPS Studies of Surface Oxidation of Metal Carbides. *Fullerenes, Nanotubes and Carbon Nanostructures* **2022**, *30*, 718−726.

(11) Kelber, J.; Seshadri, G. Adsorbate-catalyzed Anodic Dissolution and Oxidation at Surfaces in Aqueous Solutions. *Surf. Interface Anal.* **2001**, *31*, 431−441.

(12) Balogun, K.; Chukwunenye, P.; Anwar, F.; Ganesan, A.; Adesope, Q.; Willadsen, D.; Nemšák, S.; Cundari, T. R.; Bagus, P. S.; D'Souza, F.; Kelber, J. A. Interaction of Molecular Nitrogen with Vanadium Oxide in the Absence and Presence of Water Vapor at Room Temperature: Near-ambient Pressure XPS. *J. Chem. Phys.* **2022**, *157*, 104701.

(13) Kepp, K. P. A Quantitative Scale of Oxophilicity and Thiophilicity. *Inorg. Chem.* **2016**, *55*, 9461−9470.

(14) Wu, T.; Han, M.; Zhu, X.; Wang, G.; Zhang, Y.; Zhang, H.; Zhao, H. Experimental and Theoretical Understanding on Electrochemical Activation and Inactivation Processes of $Nb_3O_7(OH)$ for Ambient Electrosynthesis of NH_3. *J. Mater. Chem. A* **2019**, *7*, 16969−16978.

(15) Huang, L.; Wu, J.; Han, P.; Al-Enizi, A.; Almutairi, T. M.; Zhang, L.; Zheng, G. NbO_2 Electrocatalyst Toward 32% Faradaic Efficiency for N_2 Fixation. *Small Methods* **2019**, *3*, 1800386.

(16) Wang, J.; Kang, S.; Zhu, X.; Wang, G.; Zhang, H. Highly ordered Nb_2O_5 Nanochannel Film with Rich Oxygen Vacancies for Electrocatalytic N_2 reduction: Inactivation and Regeneration of Electrode. *Chin. Chem. Lett.* **2021**, *32*, 2833−2836.

(17) Kong, W.; Liu, Z.; Han, J.; Xia, L.; Wang, Y.; Liu, Q.; Shi, X.; Wu, Y.; Xu, Y.; Sun, X. Ambient Electrochemical N_2-to-NH_3 fixation Enabled by Nb_2O_5 Nanowire Array. *Inorg. Chem. Front.* **2019**, *6*, 423−427.

(18) Han, J.; Liu, Z.; Ma, Y.; Cui, G.; Xie, F.; Wang, F.; Wu, Y.; Gao, S.; Xu, Y.; Sun, X. Ambient N_2 Fixation to NH_3 at Ambient Conditions: Using Nb_2O_5 Nanofiber as a High-performance Electrocatalyst. *Nano Energy* **2018**, *52*, 264−270.

(19) Balogun, K.; Ganesan, A.; Chukwunenye, P.; Gharaee, M.; Adesope, Q.; Nemšák, S.; Bagus, P. S.; Cundari, T. R.; D'Souza, F.; Kelber, J. A. Vanadium Oxide, Vanadium Oxynitride, and Cobalt Oxynitride as Electrocatalysts for the Nitrogen Reduction Reaction: a Review of Recent Developments. *J. Phys.: Cond. Matter* **2023**, *35*, 333002.

(20) Jones, J. C.; Rajendran, S.; Pilli, A.; Lee, V.; Chugh, N.; Arava, L. M. R.; Kelber, J. A. In situ X-ray Photoelectron Spectroscopy Study of Lithium Carbonate Removal from Garnet-type Solid-State Electrolyte using Ultra High Vacuum Techniques. *J. Vac. Sci. Technol. A* **2020**, *38*, 023201.

(21) Briggs, D.; Seah, M. P. *Practical Surface Analysis, Auger and X-ray Photoelectron Spectroscopy*; Practical Surface Analysis; Wiley, 1990.

(22) Gupta, A.; Brar, L. K.; Pandey, O. P. Influence of Laboratory and Waste Grade Cellulose Acetate on Photo and Electrocatalytic properties of NbC_xO_y/C and NbC/C Nanocomposites. *Sol. Energy* **2019**, *189*, 120−130.

(23) Klug, J. A.; Proslier, T.; Elam, J. W.; Cook, R. E.; Hiller, J. M.; Claus, H.; Becker, N. G.; Pellin, M. J. Atomic Layer Deposition of Amorphous Niobium Carbide-Based Thin Film Superconductors. *J. Phys. Chem. C* **2011**, *115*, 25063−25071.

(24) Luo, H.; Pour Yazdi, M. A.; Chen, S.; Sun, H.; Gao, F.; Heintz, O.; de Monteynard, A.; Sanchette, F.; Billard, A. Structure, Mechanical and Tribological Properties, and Oxidation Resistance of TaC/a-C:H films Deposited by High Power Impulse Magnetron Sputtering. *Ceram. Int.* **2020**, *46*, 24986−25000.

(25) Chang, Y.; Huang, H.; Chen, Y.; Hsu, J.; Shieh, T.; Tsai, M. Biological Characteristics of the MG-63 Human Osteosarcoma Cells on Composite Tantalum Carbide/Amorphous Carbon Films. *PLoS One* **2014**, *9*, No. e95590.

(26) Darlinski, A.; Halbritter, J. Angle-resolved XPS Studies of Oxides at NbN, NbC, and Nb surfaces. *Surf. Interface Anal.* **1987**, *10*, 223−237.

(27) Kowalski, B. J.; Orłowski, B. A.; Ghijsen, J. XPS study of CdTe (110) Surface Oxidation Process. *Surf. Sci.* **1998**, *412*−*413*, 544.

(28) Halim, J.; Cook, K. M.; Naguib, M.; Eklund, P.; Gogotsi, Y.; Rosen, J.; Barsoum, M. W. X-ray Photoelectron Spectroscopy of Select Multi-Layered Transition Metal Carbides (MXenes). *Appl. Surf. Sci.* **2016**, *362*, 406−417.

(29) Islam, K.; Sultana, R.; Satpati, B.; Chakraborty, S. Studies on Structural and Dielectric Properties of NbO_2-Nb_2O_5 Thin-film-based Devices. *Vacuum* **2022**, *195*, 110675.

(30) Ivanov, M. V.; Perevalov, T. V.; Aliev, V. S.; Gritsenko, V. A.; Kaichev, V. V. Electronic structure of δ-Ta_2O_5 with Oxygen Vacancy: Ab Initio Calculations and Comparison with Experiment. *J. Appl. Phys.* **2011**, *110*, 024115.

(31) Benito, N.; Palacio, C. Nanostructuring of Ta_2O_5 Surfaces by Low Energy Ar^+ Bombardment. *Appl. Surf. Sci.* **2015**, *351*, 753−759.

(32) Bevas, C. J.; Abel, M.; Jacobs, I.; Watts, J. F. An Interfacial Chemistry Study of Methylene Diphenyl Diisocyanate and Tantalum for Heat Exchanger Applications. *Surf. Interface Anal.* **2020**, *52*, 685−693.

(33) Wolf, S.; Edmonds, M.; Sardashti, K.; Clemons, M.; Park, J. H.; Yoshida, N.; Dong, L.; Nemani, S.; Yieh, E.; Holmes, R.; Alvarez, D.; Kummel, A. C. Low-temperature Amorphous boron nitride on $Si_{0.7}Ge_{0.3}$(001), Cu, and HOPG from Sequential Exposures of N_2H_4 and BCl_3. *Appl. Surf. Sci.* **2018**, *439*, 689−696.

(34) Lawniczak-Jablonska, K.; Wolska, A.; Kuzmiuk, P.; Rejmak, P.; Kosiel, K. Local atomic Order of the Amorphous TaO_x Thin Films in Relation to their Chemical Resistivity. *RSC Adv.* **2019**, *9*, 35727−35734.

(35) Moulder, J. F.; Chastain, J.; King, R. C. *Handbook of X-ray Photoelectron Spectroscopy: A Reference Book of Standard Spectra for Identification and Interpretation of XPS Data*; Physical Electronics, 1995.

(36) Hafner, J. Ab-initio Simulations of Materials using VASP: Density-functional Theory and Beyond. *J. Comput. Chem.* **2008**, *29*, 2044−2078.

(37) Kresse, G.; Joubert, D. From Ultrasoft Pseudopotentials to the Projector Augmented-wave Method. *Phys. Rev. B* **1999**, *59*, 1758−1775.

(38) Methfessel, M.; Paxton, A. T. High-precision Sampling for Brillouin-zone Integration in Metals. *Phys. Rev. B* **1989**, *40*, 3616−3621.

(39) Grimme, S.; Antony, J.; Ehrlich, S.; Krieg, H. A Consistent and Accurate Ab Initio Parametrization of Density Functional Dispersion

Correction (DFT-D) for the 94 elements H-Pu. *J. Chem. Phys.* **2010**, *132*, 154104.

(40) Becke, A.; Johnson, E. Exchange-Hole Dipole Moment and the Dispersion Interaction: High-order Dispersion Coefficients. *J. Chem. Phys.* **2006**, *124*, 014104.

(41) Ederer, J.; Janoš, P.; Ecorchard, P.; Tolasz, J.; Štengl, V.; Beneš, H.; Perchacz, M.; Pop-Georgievski, O. Determination of Amino Groups on Functionalized Graphene Oxide for Polyurethane Nanomaterials: XPS Quantitation vs. Functional Speciation. *RSC Adv.* **2017**, *7*, 12464−12473.

(42) Zhizhin, E. V.; Pudikov, D. A.; Rybkin, A. G.; Ul'yanov, P. G.; Shikin, A. M. Synthesis and Electronic Structure of Graphene on a Nickel Film Adsorbed on Graphite. *Phys. Solid State* **2015**, *57*, 1888−1894.

(43) Muralikrishna, S.; Sureshkumar, K.; Varley, T. S.; Nagaraju, D. H.; Ramakrishnappa, T. In situ Reduction and Functionalization of Graphene Oxide with L-cysteine for Simultaneous Electrochemical Determination of Cadmium(ii), lead(ii), copper(ii), and mercury(ii) ions. *Anal. Methods* **2014**, *6*, 8698−8705.

(44) Wu, J.; Zhao, J.; Vaidhyanathan, B.; Zhang, H.; Anshuman, A.; Nare, A.; Saremi-Yarahmadi, S. Rapid Microwave-assisted Bulk Production of High-Quality Reduced Graphene Oxide for Lithium-ion Batteries. *Materialia* **2020**, *13*, 100833.

(45) Ma, X.; Chen, Y.; Li, H.; Cui, X.; Lin, Y. Annealing-free Synthesis of Carbonaceous Nb_2O_5 Microspheres by Flame Thermal Method and Enhanced Photocatalytic Activity for Hydrogen Evolution. *Mater. Res. Bull.* **2015**, *66*, 51−58.

(46) Xiong, D.; Li, W.; Liu, L. Vertically Aligned Porous Nickel (II) Hydroxide Nanosheets Supported on Carbon Paper with Long-Term Oxygen Evolution Performance. *Chem.—Asian J.* **2017**, *12*, 543−551.

(47) Jiang, L.; Huang, Y.; Zou, Y.; Meng, C.; Xiao, Y.; Liu, H.; Wang, J. Boosting the Stability of Oxygen Vacancies in α-Co $(OH)_2$ Nanosheets with Coordination Polyhedrons as Rivets for High-Performance Alkaline Hydrogen Evolution Electrocatalyst. *Adv. Energy Mater.* **2022**, *12*, 2202351.

(48) Zhu, Y.; Dong, M.; Mao, F.; Guo, W.; Li, J.; Wang, L. Self-adaption Ta/TaC Multilayer Coating with Fine Grains: toward Excellent Corrosion Resistance in Aggressive Environment. *J. Mater. Sci.* **2021**, *56*, 14298−14313.

(49) Greczynski, G.; Hultman, L. C 1s Peak of Adventitious Carbon Aligns to the Vacuum Level: Dire Consequences for Material's Bonding Assignment by Photoelectron Spectroscopy. *ChemPhysChem* **2017**, *18*, 1507−1512.

(50) Moo, J. G. S.; Awaludin, Z.; Okajima, T.; Ohsaka, T. An XPS depth-profile Study on Electrochemically Deposited TaO_x. *J. of Solid-State Electrochem.* **2013**, *17*, 3115−3123.

(51) Marenich, A. V.; Jerome, S. V.; Cramer, C. J.; Truhlar, D. G. Charge Model 5: An Extension of Hirshfeld Population Analysis for the Accurate Description of Molecular Interactions in Gaseous and Condensed Phases. *J. Chem. Theory Comput.* **2012**, *8*, 527−541.

(52) Osonkie, A.; Ganesan, A.; Chukwunenye, P.; Anwar, F.; Balogun, K.; Gharaee, M.; Rashed, I.; Cundari, T. R.; D'Souza, F.; Kelber, J. A. Electrocatalytic Reduction of Nitrogen to Ammonia: the Roles of Lattice O and N in Reduction at Vanadium Oxynitride Surfaces. *ACS Appl. Mater. Interfaces* **2022**, *14*, 531−542.

(53) Chukwunenye, P.; Ganesan, A.; Gharaee, M.; Balogun, K.; Anwar, F.; Adesope, Q.; Cundari, T. R.; D'Souza, F.; Kelber, J. A. Electrocatalytic Selectivity for Nitrogen Reduction vs. Hydrogen Evolution: a Comparison of Vanadium and Cobalt oxynitrides at different pH values. *J. Mater. Chem. A* **2022**, *10*, 21401−21415.

(54) Golden, T. D.; Shang, Y.; Wang, Q.; Zhou, T.; Electrochemical Synthesis of Rare Earth Ceramic Oxide Coatings. In *Advanced Ceramic Processing*; Mohammed, A. M. A., Ed.; InTech, 2015; pp 85−110, DOI: 10.5772/61056, ISBN: 978-953-51-2203-6.

(55) Kayode, G. O.; Montemore, M. M. Factors Controlling Oxophilicity and Carbophilicity of Transition Metals and Main Group Metals. *J. Mater. Chem. A* **2021**, *9*, 22325−22333.